MOLECULAR KNOTS

Vernier template synthesis of molecular knots

Zoe Ashbridge[1], Elisabeth Kreidt[1], Lucian Pirvu[1], Fredrik Schaufelberger[1], Joakim Halldin Stenlid[2,3], Frank Abild-Pedersen[3], David A. Leigh[1,4]*

Molecular knots are often prepared using metal helicates to cross the strands. We found that coordinatively mismatching oligodentate ligands and metal ions provides a more effective way to synthesize larger knots using Vernier templating. Strands composed of different numbers of tridentate 2,6-pyridinedicarboxamide groups fold around nine-coordinate lanthanide (III) ions to generate strand-entangled complexes with the lowest common multiple of coordination sites for the ligand strands and metal ions. Ring-closing olefin metathesis then completes the knots. A 3:2 (ditopic strand:metal) Vernier assembly produces $+3_1\#+3_1$ and $-3_1\#-3_1$ granny knots. Vernier complexes of 3:4 (tetratopic strand:metal) stoichiometry selectively form a 378-atom-long trefoil-of-trefoils triskelion knot with 12 alternating strand crossings or, by using opposing stereochemistry at the terminus of the strand, an inverted-core triskelion knot with six alternating and six nonalternating strand crossings.

Entangling molecular strands that have robust backbones has two important consequences: (i) strand-crossing regions cannot pass through each other, blocking pathways to particular conformations and altering strand dynamics, and (ii) the structure becomes nontrivial in topological terms (i.e., each crossing can be over or under with respect to others), imparting additional stereochemical complexity (*1*, *2*). Consequently, systematic strand entanglements affect the characteristics and function of DNA (*3*), RNA (*4*), and proteins (*5*). Synthetic molecular knots with relatively simple topologies (*6*–*31*), e.g., trefoils (three crossings) and pentafoils (five crossings), show promising properties for anion binding (*6*, *7*), membrane transport (*8*), catalysis (*9*, *10*), materials (*11*), nanotherapeutics (*12*), and the kinetic stabilization of supramolecular structures (*13*). Examples of extended periodic entanglements, such as two-dimensional (2D) molecularly woven polymers (*32*–*34*), 3D woven covalent organic frameworks (*35*, *36*), and polycatenanes (*37*), have also been described. The use of circular (*16*, *17*) metal helicates offers a route to rotationally symmetric topologies with up to nine crossings. However, the internal angle between building blocks increases with cyclic array size, which can prove difficult to reconcile with normal bond angles and conformations, and to date, the only known circular helicates with more than six crossings have been derived from DNA or peptides. Accordingly, there are no strategies for synthesizing branched or extended arrays of the systematic molecular entanglements necessary for larger knotted structures and assemblies (*2*).

Vernier complexes (*38*–*45*) are formed when the number of binding sites on one component of a supramolecular complex is not an integer multiple of the number of complementary binding sites on another (Fig. 1). The mismatch favors an assembly that has a number of binding sites equal to the lowest common multiple of the numbers of sites on both components. Vernier templating has been used to form discrete multicomponent assemblies of precise size and composition from much simpler building blocks (*38*–*44*), including linear duplexes (*39*, *40*, *44*, *45*) and very large (156- to 312-atom-long loop) but topologically trivial macrocycles (*41*–*43*). Trefoil knots have previously been synthesized through the coordination of a lanthanide (III) ion to a single tritopic ligand strand incorporating three covalently tethered 2,6-pyridinedicarboxamide (pdc) (*46*, *47*) binding sites (*10*, *13*, *48*). We reasoned that combining lanthanide ions with ligand strands containing a mismatched number of pdc sites, e.g., ditopic or tetratopic strands, might generate discrete, large-but-finite extended structures (Fig. 1). However, it was unclear whether such relatively weakly binding, coordinatively mismatched strands would be able to pay the entropic cost of forming a single, discrete multicomponent complex, particularly one requiring ordered entanglements. Furthermore, although point chirality of the pdc units controls the topological chirality of trefoil knots when folding a single ligand strand (Fig. 1A) (*10*, *13*, *48*), it would be more demanding to do so with multiple strands entwined around and between multiple metal ions.

Ditopic ligand strand $(R)_4$-**L1**, where $(R)_4$ refers to the four (*R*)-configured asymmetric centers of the two pdc units, was synthesized as described in the supplementary materials (section 4). Three molar equivalents of $(R)_4$-**L1** were treated with two molar equivalents of $Lu(CF_3SO_3)_3$ at 80°C in MeCN (Fig. 2A). A 3:2 strand:metal ion Vernier complex $((R)_4$-**L1**$)_3$•$[Lu]_2$ formed gradually over 3 days, as evidenced by electrospray ionization mass spectrometry (ESI-MS, *m/z* $((R)_4$-**L1**$)_3$•$[Lu]_2[CF_3SO_3]_3^{3+}$ 1554.9, etc.; fig. S78) and ^{1}H nuclear magnetic resonance (NMR) spectroscopy (Fig. 2C). Compared with the folding of an overhand trefoil knot (*10*, *48*), the formation of an open granny knot complex would likely require considerably more miscoordinated and misfolded intermediates to be unraveled and error corrected during the thermodynamically controlled assembly process. This complexity is reflected in the approximately sixfold increase in reaction time necessary to form $((R)_4$-**L1**$)_3$•$[Lu]_2$ compared with open trefoil knots tied by Ln-coordinated entangling of a single strand (*10*, *11*, *13*, *48*).

The ^{1}H NMR spectrum of $((R)_4$-**L1**$)_3$•$[Lu]_2$ shows distinctive features characteristic of an entangled geometry (*10*, *11*, *13*, *48*), such as a large upfield shift of the pyridine protons H_A and H_B caused by the shielding effects of enforced proximity to the electron-rich naphthol groups (Fig. 2C). Two sets of strand signals in a 2:1 ratio, e.g., H_A at 6.0 and 7.0 ppm, result from the structure of the Vernier assembly. Pyridine protons (e.g., H_A) of the two wrapping strands of the open knot (blue and orange strands in Fig. 2C) are less shielded than those of the wrapped strand (green), likely because of the increased conformational freedom at the strands' termini and the different pinching effect of the glycol linker (*48*). The substantial diastereotopic splitting of H_B and H_D indicate that protons in the open granny knot experience a stronger influence of the chiral environment than the symmetrical (other than the point-chiral centers) uncoordinated strands. Diffusion-ordered spectroscopy (DOSY) confirmed that a single species was present at the end of the Vernier assembly process (fig. S64).

The Vernier complex $((R)_4$-**L1**$)_3$•$[Lu]_2$ has six pendant terminal alkenes positioned for three sets of ring-closing olefin metathesis (RCM). Upon the addition of a Hoveyda-Grubbs second-generation catalyst (*49*) to $((R)_4$-**L1**$)_3$•$[Lu]_2$ in CH_2Cl_2/CH_3NO_2 (1:1, v/v) at 50°C, the closed-loop granny knot (Λ_2)-**1**•$[Lu]_2$ formed as a single diastereomer (Fig. 2A). The mass spectrum of (Λ_2)-**1**•$[Lu]_2$ confirmed the loss of three molecules of ethene from $((R)_4$-**L1**$)_3$•$[Lu]_2$ (*m/z* (Λ_2)-**1**•$[Lu]_2[CF_3SO_3]^{5+}$ 826.8, etc.; fig. S80), with good correlation between the calculated and the observed isotope distributions (Fig. 2F). The ^{1}H NMR spectrum of (Λ_2)-**1**•$[Lu]_2$ (Fig. 2D) is consistent with the increased conformational restriction of the closed-loop knot and greater similarity of connections between the pdc environments.

The metal-coordinated granny knot (Λ_2)-**1**•$[Lu]_2$ was treated with tetraethylammonium

[1]Department of Chemistry, University of Manchester, Oxford Road, Manchester M13 9PL, UK. [2]SUNCAT Center for Interface Science and Catalysis, Department of Chemical Engineering, Stanford University, Stanford, CA 94305, USA. [3]SUNCAT Center for Interface Science and Catalysis, SLAC National Accelerator Laboratory, Menlo Park, CA 94025, USA. [4]School of Chemistry and Molecular Engineering, East China Normal University, Shanghai 200062, China.
*Corresponding author. Email: david.leigh@manchester.ac.uk

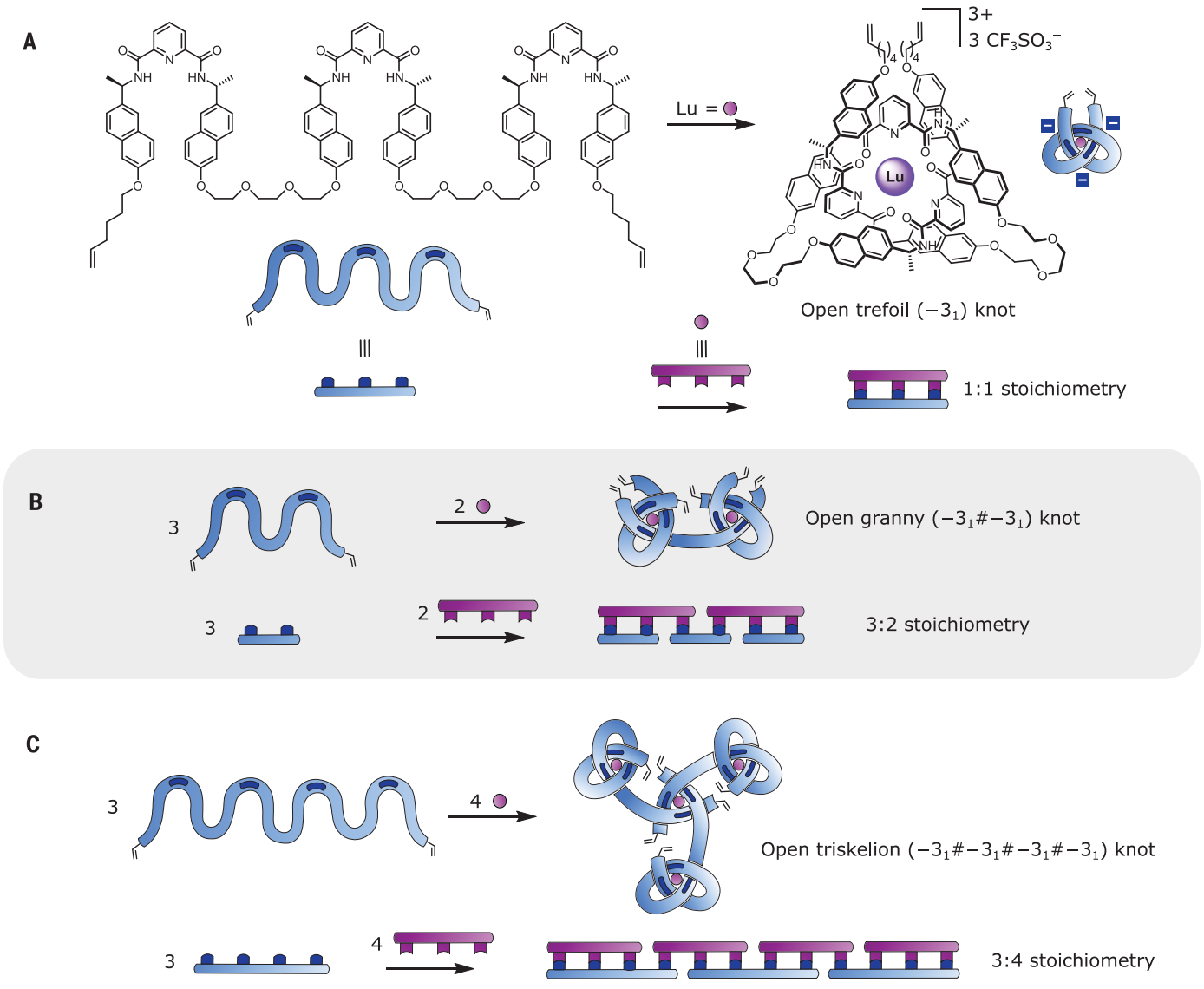

Fig. 1. Vernier template strategy for the synthesis of large molecular knots with extended arrays of entanglements. Discrete supramolecular assemblies produced by (nine-coordinate) lanthanide (III) ions (purple) binding to (tridentate) pdc sites (dark blue bars) in ligand strands (light blue). The mechanical stereochemistry of the strand crossings is programmed by the chirality of the pdc groups [dark blue bars indicate (*R*)-configured chiral centers; red bars in other figures indicate (*S*)-configuration]. The minus signs in the blue squares refer to the stereochemistry of the strand crossing formed, not to charges. (**A**) A 1:1 ratio of a single tritopic (i.e., three pdc sites) ligand to lutetium (III) ions generates a -3_1 overhand (open trefoil) knot (*10*). (**B**) A 3:2 ratio of ditopic ligand to metal ions gives a $-3_1\#-3_1$ open granny knot. (**C**) A 3:4 ratio of tetratopic ligand to metal ions gives a $-3_1\#-3_1\#-3_1\#-3_1$ open triskelion knot. Diagrams of the analogous linear Vernier complexes are shown below each knot.

fluoride (Et_4NF), and the resulting demetalated knot was isolated by size-exclusion chromatography to give (Λ_2)-**1** in 14% yield over three steps. The ^{1}H NMR spectrum of granny knot (Λ_2)-**1** is broad (Fig. 2E), consistent with chain reptation (*50*) in a tightly knotted compound (*17*), with the spectrum becoming less broadened at elevated temperatures (fig. S72). The matrix-assisted laser desorption/ionization–time-of-flight (MALDI-TOF) mass spectrum confirmed the metal-free knot to be a single species of the expected molecular mass, confirming that the three starting organic building blocks of $(R)_4$-**L1** had been incorporated into one continuous closed-loop strand (fig. S82). The metal-coordinated granny knot (Λ_2)-**1**•$[Lu]_2$ could subsequently be reformed by treating (Λ_2)-**1** with $Lu(CF_3SO_3)_3$ at 80°C in MeCN for 16 hours (supplementary materials, section 6.3, and fig. S21). The enantiomeric granny knot (Δ_2)-**1** was prepared in analogous fashion from building block $(S)_4$-**L1** (supplementary materials, section 6.4). Circular dichroism (CD) spectroscopy confirmed that the Vernier template syntheses of (Λ_2)-**1**•$[Lu]_2$ and (Δ_2)-**1**•$[Lu]_2$ proceeded with complete topological stereoselectivity, with their mirror-image chirality shown by the inverted exciton coupling maxima (Fig. 2G).

Encouraged by these results, we explored increasing the topological complexity through the use of tetratopic ligand strands. These ligands set up conditions for a coordinative mismatch with a lowest common multiple of 12. Complexing four lanthanide (III) ions with three tetratopic ligand strands should form a $3_1\#3_1\#3_1\#3_1$ open-knot Vernier complex [the # symbol denotes the connection of tangles, in this case 3_1, in the nomenclature for

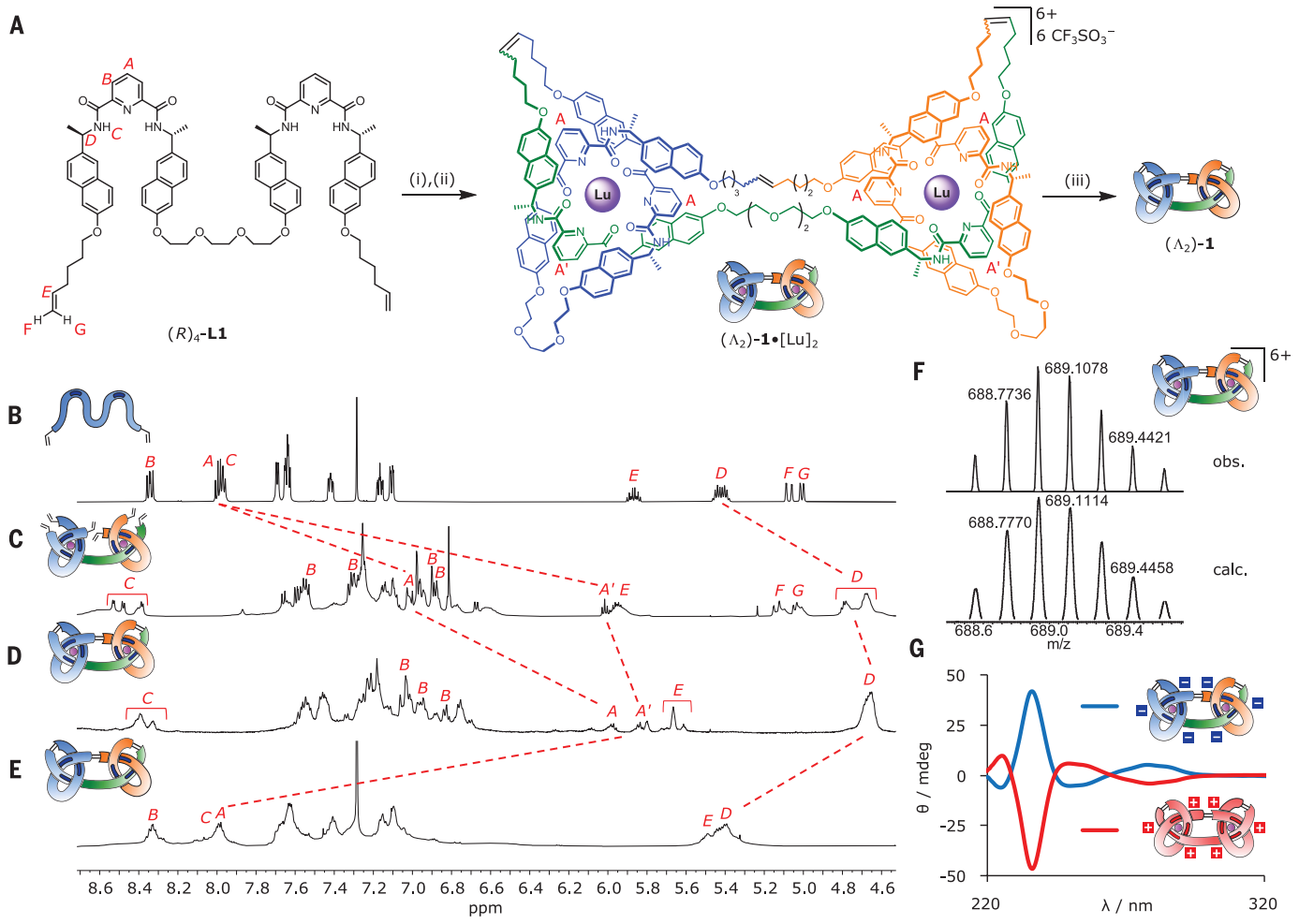

Fig. 2. Vernier (3:2, strand:metal ion) template synthesis of molecular granny knots. (**A**) Reaction conditions: (i) $Lu(CF_3SO_3)_3$, MeCN, 80°C, 72 hours; (ii) Hoveyda-Grubbs second-generation catalyst, CH_2Cl_2/CH_3NO_2 (1:1, v/v), 50°C, 16 hours; and (iii) Et_4NF, MeCN, room temperature, 1 hour, 14% over three steps. (**B** to **E**) Partial ^1H NMR spectra (600 MHz, 298 K) of granny knots and ligand precursor: (B) ditopic ligand $(R)_4$-**L1** ($CDCl_3$); (C) metal-coordinated open granny knot $((R)_4$-**L1**$)_3$•$[Lu]_2$ (CD_3CN); (D) metal-coordinated granny knot (Λ_2)-**1**•$[Lu]_2$ (CD_3CN); and (E) organic granny knot (Λ_2)-**1** ($CDCl_3$). Selected spectral assignments correspond to proton labeling in (A). Full assignments can be found in the supplementary materials. (**F**) High-resolution ESI-MS(+) of closed granny knot (Λ_2)-**1**•$[Lu]_2$ comparing the observed spectrum (top) with the calculated isotopic distribution of $[M–6(CF_3SO_3)]^{6+}$ (bottom). (**G**) Overlaid circular dichroism spectra of granny knots (Λ_2)-**1**•$[Lu]_2$ (blue) and (Δ_2)-**1**•$[Lu]_2$ (red), (0.05 mM, MeCN), normalized for absorbance. The minus and plus signs in the blue and red squares refer to the stereochemistry of the strand crossings, not to charges.

composite knots (*51*)], which could be covalently captured to yield a trefoil-of-trefoils triskelion knot (Fig. 1C). We postulated that this assembly would most likely occur in a stepwise fashion in which a single ligand first folds and entangles around one lanthanide (III) ion, leaving a loose end containing one pdc unit. Several factors (e.g., the entropic cost of lost flexibility of the strand end and stabilizing π-stacking interactions) indicate that the structure with a free pdc site at the strand terminus should be thermodynamically favored over an uncoordinated internal pdc unit; proton NMR confirmed this to be the case (supplementary materials, section 12). Three such intermediates can bind to a fourth lanthanide ion, forming a central trimeric circular helicate, with the resulting Vernier complex fulfilling the coordination requirements for three ligand strands and four metal ions (Fig. 1C).

Tetratopic ligand strand $(R)_8$-**L2** was synthesized as detailed in the supplementary materials (section 4). Treatment of $(R)_8$-**L2** with either $Lu(CF_3SO_3)_3$ or $Yb(CF_3SO_3)_3$ in a 3:4 strand:metal ratio at 80°C in MeCN generated the corresponding Vernier open triskelion complexes $((R)_8$-**L2**$)_3$•$[Lu/Yb]_4$ in 7 days (Fig. 3A). The ESI mass spectrum of $((R)_8$-**L2**$)_3$•$[Lu]_4$ confirmed a 3:4 ligand-to-metal ratio (m/z $((R)_8$-**L2**$)_3$•$[Lu]_4[CF_3SO_3]_7^{5+}$ 1865.7, etc.; fig. S84), with good correlation between calculated and observed isotope distributions (Fig. 3B). DOSY showed the Vernier complexes to be single discrete species (fig. S68).

The ^1H NMR spectrum of $((R)_8$-**L2**$)_3$•$[Lu]_4$ is broad but shows characteristic upfield shifts of pyridine protons H_A and H_B upon entanglement (Fig. 4C), similar to those of the open granny knot $((R)_4$-**L1**$)_3$•$[Lu]_2$ (Fig. 2C). Both the threefold molecular symmetry of the triskelion complex and the difference in structure between the central and outer entanglement arrays are apparent from the paramagnetic shifts in the ^1H NMR spectrum of $((R)_8$-**L2**$)_3$•$[Yb]_4$ (Fig. 3C and supplementary materials, section 15). The pseudocontact shifts of nuclei close to paramagnetic lanthanide ions are highly sensitive to both the relative spatial arrangement of the observed nucleus and the lanthanide, and to the magnetic anisotropy of the lanthanide (which depends on its ligand field) (*52*, *53*). The magnetic anisotropy of a specific lanthanide can be visualized by a tensor, and individual isosurfaces of such a tensor

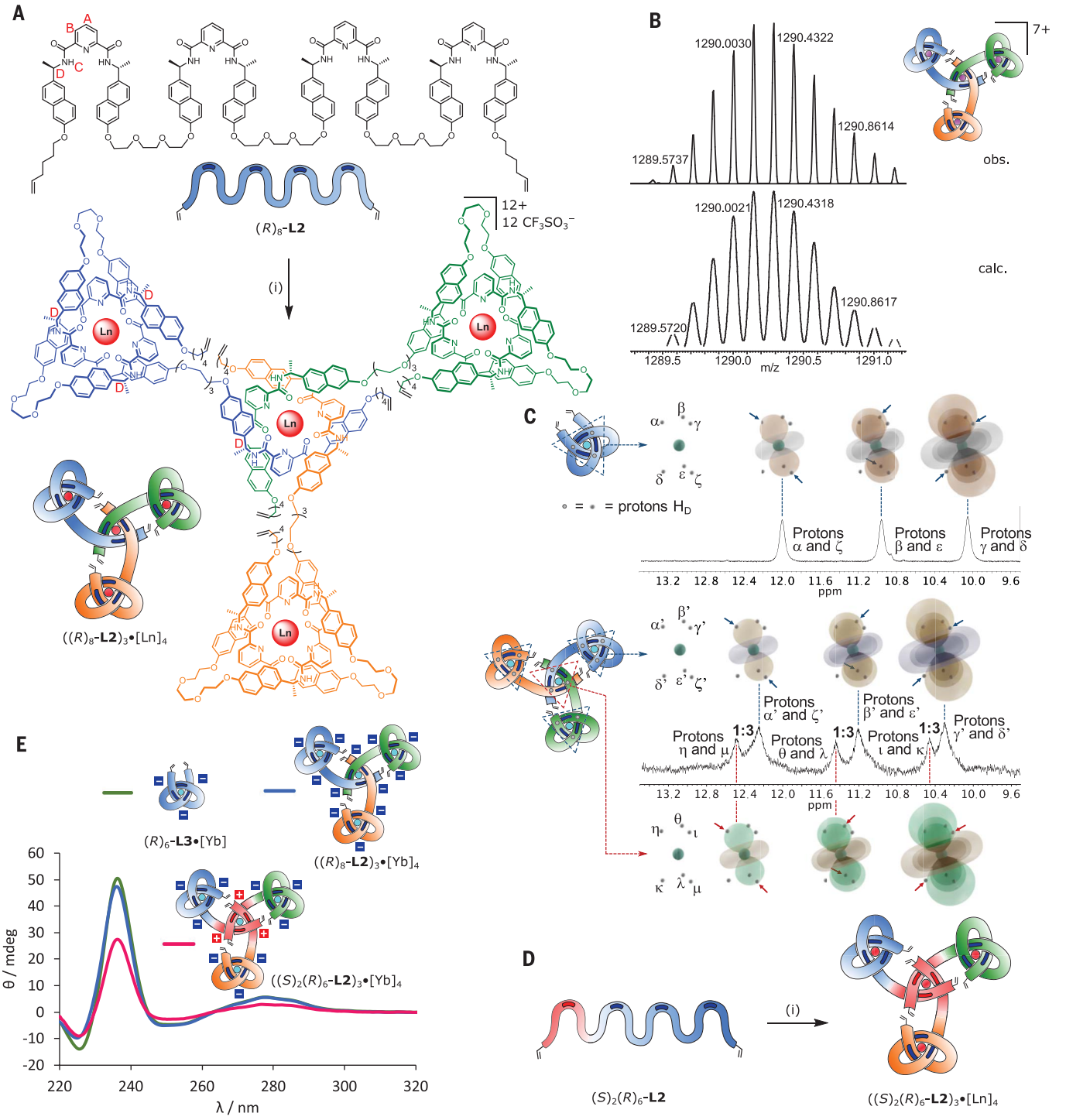

Fig. 3. Vernier (3:4, strand:metal ion) template synthesis of 12-crossing molecular triskelion open-knot complexes. (**A**) Vernier assembly of triskelion open-knot complex ((*R*)$_8$-**L2**)$_3$•[Ln]$_4$. Reaction conditions: Ln(CF$_3$SO$_3$)$_3$, MeCN, 80°C, 7 days. (**B**) High-resolution ESI-MS(+) of ((*R*)$_8$-**L2**)$_3$•[Lu]$_4$ showing the observed distribution (top) and the calculated isotopic distribution (bottom) of [M–7(CF$_3$SO$_3$)]$^{7+}$. (**C**) Partial ^{1}H NMR spectra (CD$_3$CN, 600 MHz, 298 K) of open trefoil knot (*R*)$_6$-**L3**•[Yb] (top) and open triskelion knot ((*R*)$_8$-**L2**)$_3$•[Yb]$_4$ (bottom) showing the paramagnetic shifted H$_D$ protons. Protons located on the most compact isoshift surface of the tensor experience the largest shift; protons on the most expanded isoshift surface experience the smallest shift. The observed pattern for ((*R*)$_8$-**L2**)$_3$•[Yb]$_4$ reflects the geometry and topology of the complex (supplementary materials, section 8). (**D**) Vernier assembly of inverted core triskelion open-knot complex ((*S*)$_2$(*R*)$_6$-**L2**)$_3$•[Ln]$_4$. Reaction conditions: Ln(CF$_3$SO$_3$)$_3$, MeCN, 80°C, 7 days. (**E**) Overlaid circular dichroism spectra of Yb (III) triskelion and inverted core triskelion open-knot complexes and overhand knot: (*R*)$_6$-**L3**•[Yb] (green), ((*R*)$_8$-**L2**)$_3$•[Yb]$_4$ (blue), and ((*S*)$_2$(*R*)$_6$-**L2**)$_3$•[Yb]$_4$ (red), (0.05 mM, MeCN), normalized for absorbance. The minus and plus signs in the blue and red squares refer to the stereochemistry of the strand crossings, not to charges.

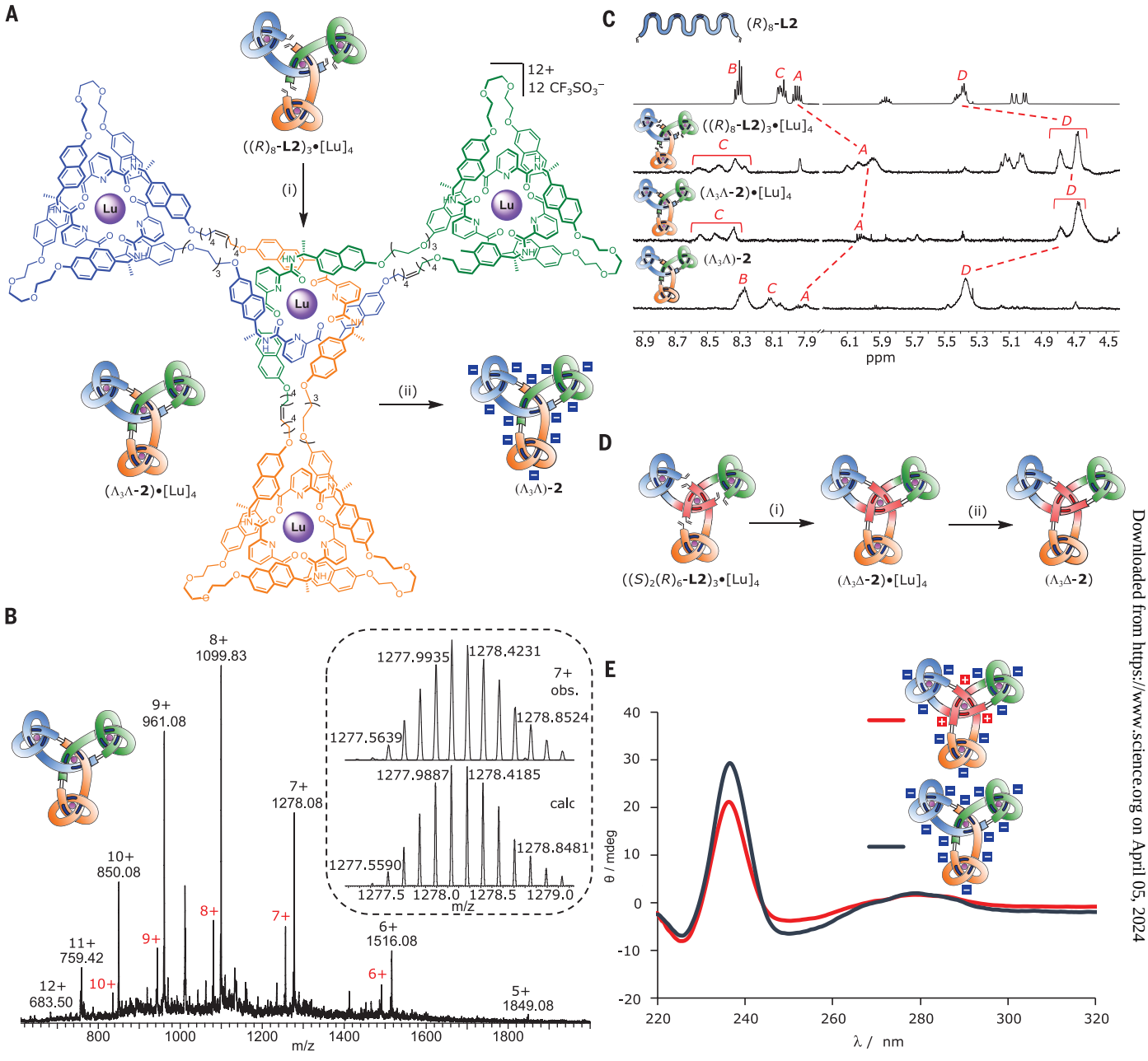

Fig. 4. Formation of closed-loop 12-crossing molecular triskelion knots. (**A**) Reaction conditions: (i) Hoveyda-Grubbs second-generation catalyst, CH_2Cl_2/CH_3NO_2 (1:1, v/v), 50°C, 16 hours, and (ii) Et_4NF, MeCN, room temperature, 1 hour, 6% over three steps. (**B**) Low-resolution ESI-MS(+) of closed triskelion knot ($\Lambda_3\Lambda$)-**2**•$[Lu]_4$, with ions observed either as $[M–n(CF_3SO_3)]^{n+}$ adducts (black) or $[M–(n+1)(CF_3SO_3)+H^-]^{n+}$ adducts (red). Inset: Comparison of observed high-resolution spectrum (top) with the calculated isotopic distribution of $[M–7(CF_3SO_3)]^{7+}$ (bottom). (**C**) Partial ^1H NMR spectra (600 MHz, 298 K) of triskelion knot and ligand precursor: $(R)_8$-**L2** ($CDCl_3$), $((R)_8$-**L2**$)_3$•$[Lu]_4$ (MeCN), (Λ_3,Λ)-**2**•$[Lu]_4$ (MeCN), and (Λ_3,Λ)-**2** ($CDCl_3$). Spectral assignments correspond to proton labeling in Fig. 3A. Full assignments can be found in the supplementary materials. (**D**) Reaction conditions: (i) Hoveyda-Grubbs second-generation catalyst, CH_2Cl_2/CH_3NO_2 (1:1, v/v), 50°C, 16 hours, and (ii) Et_4NF, MeCN, room temperature, 1 hour, 8% over three steps. (**E**) Overlaid circular dichroism spectra of remetalated triskelion knots (Λ_3,Λ)-**2**•$[Lu]_4$ (blue) and (Λ_3,Δ)-**2**•$[Lu]_4$ (red) (0.05 mM, MeCN), normalized for absorbance. The minus and plus signs in the blue and red squares refer to the stereochemistry of the strand crossings, not to charges.

relate to certain pseudocontact shifts of nuclei located on these surfaces. Nuclei located on the same isosurface experience the same pseudocontact shift. In a Yb (III)–coordinated control compound (open trefoil complex $(R)_6$-**L3**•[Yb]), the H_D protons bound to the carbon stereocenters, identified by heteronuclear single quantum coherence correlation (fig. S127), appear as three, equal-intensity, strongly shifted signals (Fig. 3C, top spectrum). This feature indicates that the six H_D protons are located pairwise on three different isosurfaces of the tensor. In the Yb (III) open triskelion complex ($(R)_8$-**L2**$)_3$•$[Yb]_4$, the H_D protons appear as two sets of three signals in a 1:3 intensity ratio (Fig. 3C, bottom spectrum), with the most intense set of signals almost coincident with the chemical shifts of those of the open trefoil complex $(R)_6$-**L3**•[Yb]. The 1:3 ratio reflects both the central:outer ratio of metal environments in the open triskelion knot and

the symmetry of the supramolecular Vernier complex. The 1:3 ratio of environments also rules out alternative structures, such as a cyclic tetratrefoil shield knot (supplementary materials, section 12) or link-like assemblies in which the pdc unit of a strand used to bind the bridging second metal ion is one of the internal sites.

The open-knot Vernier complexes were also characterized by circular dichroism (Fig. 3E). The overall appearance of the CD spectrum of the open triskelion complex $((R)_8$-**L2**$)_3$•$[Yb]_4$ (blue) closely resembles that of the Λ-open trefoil complex $(R)_6$-**L3**•[Yb] (green), and the spectra are almost identical when normalized for the fourfold number of chromophores in $((R)_8$-**L2**$)_3$•$[Yb]_4$. The small differences between the two can be attributed to the different chiral expression of the central entangled feature of $((R)_8$-**L2**$)_3$•$[Yb]_4$, which lacks the folded loops of the outer trefoil tangles (*48*).

Multiple tethered pdc groups cannot assemble around a single lanthanide (III) ion with tethered pdc groups of opposing stereochemistry because of steric clashes (supplementary materials, section 5). Because strand-crossing stereochemistry is governed by the point chirality in the pdc groups, this offers the possibility of a new element of selection and control in assembling Vernier complexes. To explore this, we prepared a diastereomeric ligand strand of $(R)_8$-**L2** in which one terminal pdc unit had the (*S*,*S*)-stereochemistry, namely $(S)_2(R)_6$-**L2** (supplementary materials, section 4). Treatment of $(S)_2(R)_6$-**L2** with $Lu(CF_3SO_3)_3$ or $Yb(CF_3SO_3)_3$ in a 3:4 strand: metal ion ratio at 80°C in MeCN generated the corresponding Vernier open inverted core triskelion complexes $((S)_2(R)_8$-**L2**$)_3$•$[Lu]_4$ and $((S)_2(R)_8$-**L2**$)_3$•$[Yb]_4$ over 7 days (Fig. 3D). Mass spectrometry confirmed the 3:4 ligand-to-metal ratio of the resulting supramolecular structures (fig. S25).

The CD spectrum of $((S)_2(R)_6$-**L2**$)_3$•$[Yb]_4$ (Fig. 3E, red) is consistent with the structure being the inverted core triskelion knot with three outer Λ entanglements and a central Δ entanglement. The inverted exciton coupling of the central Δ entanglement compensates for the intensity of the coupling of one of the outer Λ entanglements, leading to an intensity for the inverted core triskelion of approximately half that of the all-Λ open triskelion complex $((R)_8$-**L2**$)_3$•$[Yb]_4$ (Fig. 3E, red).

Closure of $((R)_8$-**L2**$)_3$•$[Lu]_4$ by RCM, subsequent demetallation by Et_4NF, and size-exclusion chromatography gave the metal-free organic knot (Λ_3,Λ)-**2** in 6% isolated yield over three steps (Fig. 4A) as a single species as determined by DOSY (fig. S70). The broadness of the ^{1}H NMR spectrum of (Λ_3,Λ)-**2** (Fig. 4C) only reduced noticeably at 348 K (fig. S73), reflecting the degree and congestion of strand entanglement. The most abundant ion in the MALDI-TOF spectrum at *m/z* 7535 corresponds to the organic knot (fig. S88). The isolated organic knot could be remetalated by treatment with an excess of $Lu(CF_3SO_3)_3$ over 48 hours in $MeCN/CDCl_3$ (4:1, v/v) to form (Λ_3,Λ)-**2**•$[Lu]_4$ in 92% yield (supplementary materials, section 7.3). ESI-MS of the regenerated (Λ_3,Λ)-**2**•$[Lu]_4$ shows a pristine spectrum with molecular ion charges ranging from 12+ to 5+ (Fig. 4B). The corresponding inverted core triskelion complex $((S)_2(R)_6$-**L2**$)_3$•$[Lu]_4$ was also closed by RCM and demetalated by Et_4NF to give (Λ_3,Δ)-**2** (Fig. 4D). The normalized CD spectrum of closed knot (Λ_3,Δ)-**2**•$[Lu]_4$ shows the expected reduction in intensity compared with (Λ_3,Λ)-**2**•$[Lu]_4$ as a result of the chirality of the central Δ-handed fragment (Fig. 4E and supplementary materials, section 11).

Although the triskelion knot (Λ_3,Λ)-**2** and inverted core triskelion knot (Λ_3,Δ)-**2** both have 12 crossings, their topologies are distinctly different. Triskelion knot (Λ_3,Λ)-**2** has 12 alternating crossings, meaning that for each crossing, the thread must formally traverse from one face of the loop to the other and back again; however, (Λ_3,Δ)-**2** has six alternating and six nonalternating crossings, the latter crossings achievable by the strand lying across two adjacent sections of the loop. This greatly affects the intrinsic tightness of the isomeric knots, as reflected in their approximate hydrodynamic radii measured by DOSY ((Λ_3,Λ)-**2** 2.03 nm, (Λ_3,Δ)-**2** 2.73 nm, $CDCl_3$, 298 K; supplementary materials, section 9.2, and table S3).

The C_3-symmetric triskelion conformation of (Λ_3,Λ)-**2**•$[Lu]_4$ was calculated to be ~150 kcal/mol more stable than other tangled conformers (supplementary materials, section 14), a symmetry consistent with the 1:3 signal intensities observed for the H_D protons in the ^{1}H NMR spectrum of $((R)_8$-**L2**$)_3$•$[Yb]_4$. The stability was estimated by condensed-phase hybrid density-functional theory calculations [PCM-B3LYP-D3(BJ)/def2-SV(P), with effective core potentials for Lu, using ORCA 4.2.1] on low-energy structures identified by an extensive simulated annealing-based structural search protocol (*28*) (supplementary materials, section 14). Other than being flexible about the chains that link the trefoil tangles to the central core, the metal-coordinated triskelion knot adopts a well-defined 2D conformation despite being composed of a single continuous self-entangled 1D strand. We note a fundamental similarity to the structure of knitted materials (*54*), which arise from the systematic self-entanglement of a single 1D strand in a pattern that results in a 2D layer that can adopt complex 3D curvature (like a knitted hat or sweater). This differs from weaving (*32*–*36*), which results in the periodic mutual entanglement of multiple 1D strands.

In summary, Vernier template synthesis is a powerful tool for constructing large molecular structures with complex systematic networks of entanglements. Granny knots (six alternating crossings) were accessed from a 3:2 Vernier complex, and a triskelion knot with 12 alternating crossings and an inverted-core triskelion knot with six alternating and six nonalternating crossings was accessed from 3:4 Vernier complexes. The latter, 378-atom-long closed-loop knots (~40 nm strand length) are among the largest discrete macrocycles synthesized to date, with the added complexity of defined sequences of stereocontrolled strand entanglements, the precise topology affecting the structure and properties of the resulting knots. Both types of triskelion knot topologies are common motifs in extended Hiberno-Saxon knotwork and interlace (*55*). The ability to synthesize large, hierarchically knotted molecular architectures with precise control of entanglements, crossing stereochemistry, and overall symmetry presents opportunities and research directions for topological molecules and materials.

REFERENCES AND NOTES

1. S. D. P. Fielden, D. A. Leigh, S. L. Woltering, *Angew. Chem. Int. Ed.* **56**, 11166–11194 (2017).
2. J. F. Stoddart, *Nano Lett.* **20**, 5597–5600 (2020).
3. D. Meluzzi, D. E. Smith, G. Arya, *Annu. Rev. Biophys.* **39**, 349–366 (2010).
4. M. Zhao, M. T. Woodside, *Nat. Chem. Biol.* **17**, 975–981 (2021).
5. N. C. H. Lim, S. E. Jackson, *J. Phys. Condens. Matter* **27**, 354101 (2015).
6. J.-F. Ayme *et al.*, *J. Am. Chem. Soc.* **137**, 9812–9815 (2015).
7. R. A. Bilbeisi *et al.*, *Chem. Sci.* **7**, 2524–2531 (2016).
8. D. P. August *et al.*, *J. Am. Chem. Soc.* **142**, 18859–18865 (2020).
9. V. Marcos *et al.*, *Science* **352**, 1555–1559 (2016).
10. G. Gil-Ramírez *et al.*, *J. Am. Chem. Soc.* **138**, 13159–13162 (2016).
11. N. Katsonis *et al.*, *Nat. Chem.* **12**, 939–944 (2020).
12. F. Benyettou *et al.*, *Chem. Sci.* **10**, 5884–5892 (2019).
13. D. A. Leigh, L. Pirvu, F. Schaufelberger, D. J. Tetlow, L. Zhang, *Angew. Chem. Int. Ed.* **57**, 10484–10488 (2018).
14. C. O. Dietrich-Buchecker, J.-P. Sauvage, *Angew. Chem. Int. Ed.* **28**, 189–192 (1989).
15. J.-P. Sauvage, *Angew. Chem. Int. Ed.* **56**, 11080–11093 (2017).
16. J.-F. Ayme *et al.*, *Nat. Chem.* **4**, 15–20 (2011).
17. J. J. Danon *et al.*, *Science* **355**, 159–162 (2017).
18. J. P. Carpenter *et al.*, *Chem* **7**, 1534–1543 (2021).
19. Y. Inomata, T. Sawada, M. Fujita, *Chem* **6**, 294–303 (2020).
20. Y. Inomata, T. Sawada, M. Fujita, *J. Am. Chem. Soc.* **143**, 16734–16739 (2021).
21. H.-N. Zhang, W.-X. Gao, Y.-J. Lin, G.-X. Jin, *J. Am. Chem. Soc.* **141**, 16057–16063 (2019).
22. L.-L. Dang, H.-J. Feng, Y.-J. Lin, G.-X. Jin, *J. Am. Chem. Soc.* **142**, 18946–18954 (2020).
23. Z. Cui, Y. Lu, X. Gao, H.-J. Feng, G.-X. Jin, *J. Am. Chem. Soc.* **142**, 13667–13671 (2020).
24. D. A. Leigh *et al.*, *Nat. Chem.* **13**, 117–122 (2021).
25. Y. Segawa *et al.*, *Science* **365**, 272–276 (2019).
26. H. Adams *et al.*, *Nature* **411**, 763 (2001).
27. P. E. Barran *et al.*, *Angew. Chem. Int. Ed.* **50**, 12280–12284 (2011).
28. D. A. Leigh *et al.*, *Nature* **584**, 562–568 (2020).
29. J. Brüggemann *et al.*, *Angew. Chem. Int. Ed.* **46**, 254–259 (2007).
30. N. Ponnuswamy, F. B. L. Cougnon, J. M. Clough, G. D. Pantoş, J. K. M. Sanders, *Science* **338**, 783–785 (2012).
31. F. B. L. Cougnon, K. Caprice, M. Pupier, A. Bauzá, A. Frontera, *J. Am. Chem. Soc.* **140**, 12442–12450 (2018).
32. U. Lewandowska *et al.*, *Nat. Chem.* **9**, 1068–1072 (2017).
33. Z. Wang *et al.*, *Nat. Commun.* **8**, 14442 (2017).
34. D. P. August *et al.*, *Nature* **588**, 429–435 (2020).
35. Y. Liu *et al.*, *Science* **351**, 365–369 (2016).
36. Y. Liu *et al.*, *J. Am. Chem. Soc.* **140**, 16015–16019 (2018).
37. Q. Wu *et al.*, *Science* **358**, 1434–1439 (2017).
38. J. S. Lindsey, *New J. Chem.* **15**, 153–180 (1991).
39. T. R. Kelly, R. L. Xie, C. Kraebel Weinreb, T. Bregant, *Tetrahedron Lett.* **39**, 3675–3678 (1998).
40. C. A. Hunter, S. Tomas, *J. Am. Chem. Soc.* **128**, 8975–8979 (2006).
41. M. C. O'Sullivan *et al.*, *Nature* **469**, 72–75 (2011).

42. D. V. Kondratuk *et al*., *Angew. Chem. Int. Ed.* **51**, 6696–6699 (2012).
43. D. V. Kondratuk *et al*., *Chem. Eur. J.* **20**, 12826–12834 (2014).
44. X. Li, C. Hao, C. Tian, P. Wang, C. Mao, *Chem. Commun.* **50**, 6361–6363 (2014).
45. T. Wei, J. H. Jung, T. F. Scott, *J. Am. Chem. Soc.* **137**, 16196–16202 (2015).
46. D. E. Barry, D. F. Caffrey, T. Gunnlaugsson, *Chem. Soc. Rev.* **45**, 3244–3274 (2016).
47. D. E. Barry *et al*., *Inorg. Chem.* **59**, 2646–2650 (2020).
48. Y. Song *et al*., *Chem. Sci.* **12**, 1826–1833 (2021).
49. S. B. Garber, J. S. Kingsbury, B. L. Gray, A. H. Hoveyda, *J. Am. Chem. Soc.* **122**, 8168–8179 (2000).
50. P. G. de Gennes, *J. Chem. Phys.* **55**, 572–579 (1971).
51. C. C. Adams, *The Knot Book* (Freeman, 1994).
52. G. Otting, *Annu. Rev. Biophys.* **39**, 387–405 (2010).
53. W.-M. Liu, M. Overhand, M. Ubbink, *Coord. Chem. Rev.* **273–274**, 2–12 (2014).
54. S. G. Markande, E. A. Matsumoto, Knotty knits are tangles on tori. arXiv:2002.01497v1 [cond-mat.soft] (2020).
55. R. Megaw, V. Megaw, *Celtic Art: From Its Beginnings to the Book of Kells* (Thames & Hudson, 1989).

ACKNOWLEDGMENTS

We thank the University of Manchester Mass Spectrometry Service Centre (G. Smith and E. Enston) for MALDI-TOF and high-resolution mass spectrometry, the Swedish National Infrastructure for Computing at the National Supercomputer Centre of Linköping University and Stanford University and the Stanford Research Computing Center for computational resources, and J.-F. Lemonnier and S. Borsley for useful discussions. **Funding:** This work was supported by the Engineering and Physical Sciences Research Council (EPSRC grant EP/P027067/1); the European Research Council (ERC advanced grant 786630); Marie Skłodowska-Curie Actions of the European Union (individual postdoctoral fellowship EC 746993 to F.S.); the German Research Foundation (DFG individual postdoctoral fellowship to E.K.); the Knut and Alice Wallenberg Foundation (individual postdoctoral fellowship 2019.0586 to J.H.S.); and the US Department of Energy, Office of Science, Office of Basic Energy Sciences, Chemical Sciences, Geosciences, and Biosciences Division, Catalysis Science Program to the SUNCAT Center for Interface Science and Catalysis (F.A.-P.). D.A.L. is a Royal Society research professor. **Author contributions:** Z.A., E.K., L.P., and F.S. planned and completed the synthetic work. J.H.S. and F.A.-P. performed computational investigations. D.A.L. directed the research. Z.A., E.K., L.P., F.S., J.H.S., F.A.-P., and D.A.L. analyzed the results and wrote the manuscript. **Competing interests:** The authors declare no competing interests. **Data and materials availability:** All data are available in the main text or the supplementary materials.

SUPPLEMENTARY MATERIALS

science.org/doi/10.1126/science.abm9247
Supplementary Text
Figs. S1 to S128
Tables S1 to S3
References (*56*–*81*)

21 October 2021; accepted 1 February 2022
10.1126/science.abm9247